Using Single-view Observations of Cometary Plasma Tails to Infer Solar Wind Speed

Long Cheng[1,2] , Yuming Wang[1,2] , and Xiaolei Li[1,2]
[1] CAS Key Laboratory of Geospace Environment, School of Earth and Space Sciences, University of Science and Technology of China, Hefei 230026, People's Republic of China; ymwang@ustc.edu.cn
[2] CAS Center for Excellence in Comparative Planetology, University of Science and Technology of China, Hefei 230026, People's Republic of China

Abstract

A comet plasma tail is a product of the interaction between the solar wind and the comet's coma, and has long been studied as a natural probe of the solar wind condition. We previously developed a method to derive the solar wind speed from dual-view observations of comet plasma tails. Here we improve the method to use single-view observations by assuming a radially propagating solar wind and apply it to two comets, C/2011 W3 (Lovejoy) and C/2012 S1 (ISON) observed by coronagraphs on board the Solar and Heliospheric Observatory and STEREO. We compare the results to the solar wind simulations and tomography and to the results from our previous dual-view method, and find they are generally consistent, especially when the comets were far away from the Sun or far away from the ecliptic plane and when the observer is high above the comet's orbital plane. Meanwhile, we notice that this method may suffer from a large error for comets near the ecliptic plane and close to the Sun, where a nonradial component of the solar wind is significant. Using the observations from the first seven orbits of the Parker Solar Probe, we show that the solar wind deviates from a radial direction significantly within around 35 R_s. We also notice that, when the nonradial solar wind component is presented, the error may be even larger if the observer is closer to the comet's orbital plane. This method provides a potentially useful tool to estimate the solar wind speed around comets from only single-view imaging observations.

Unified Astronomy Thesaurus concepts: Solar wind (1534); Comet tails (274)

1. Introduction

The solar wind is the plasma that is ejected by the Sun to the corona and propagates into interplanetary space (Cranmer et al. 2017). Measurements of the speed of the solar wind are crucial to understand its acceleration in the corona and its spreading in the heliosphere (Hansteen & Leer 1995). Methods to learn solar wind speeds include direct detections and indirect estimations from remote observations. In situ solar wind speed is measured by particle detectors on spacecraft. Most in situ measurements are near Earth orbit, such as by the Advanced Composition Explorer (Acuña et al. 1995; Stone et al. 1998) and Wind (Ogilvie & Desch 1997); they only provide information on the solar wind at 1 au and in the ecliptic plane. There are also some measurements at high latitudes such as by Ulysses (Wenzel & Smith 1992), in regions near the Sun by the Parker Solar Probe (PSP; Fox et al. 2016), and at other distances from the Sun by spacecraft near other planets, like Venus Express (Titov et al. 2006), Mars Express (Chicarro et al. 2004), the Mars Atmosphere and Volatile Evolution mission (Jakosky et al. 2015), Juno (Bolton et al. 2017), Cassini (Matson et al. 2002), etc. The solar wind speed could also be estimated indirectly by remote sensing from coronagraphs or ground-based observations. Data from heliospheric tomography using ground-based interplanetary scintillation (IPS) could be used to reconstruct the solar wind structures on relatively low spatial and temporal scales (Bisi et al. 2009). Coronagraphic data from the Large Angle and Spectrometric Coronagraph Experiment on board the Solar and Heliospheric Observatory (SOHO; Domingo et al. 1995) and the HI1 on board the Solar Terrestrial Relations Observatory (STEREO; Kaiser 2005) could also be used to infer the two-dimensional solar wind speed by using Fourier filtering (Cho et al. 2018) or by tracing the propagation of blobs or coronal mass ejections (Li et al. 2021).

Comets are natural probes in the heliosphere, covering a broad spatial distribution in latitude and distance to the Sun, and may provide nearly in situ measurement of the coronal magnetic field (Downs et al. 2013) and turbulence in the solar wind (DeForest et al. 2015). A comet plasma tail is formed by plasma originating near the comet that is swept by the solar wind (Swamy 2010). Buffington et al. (2008) and Clover et al. (2010) tracked the plasmoid motion along the radial solar wind direction to estimate the ambient solar wind speed along the plasma tail. While oscillation of the plasma tail means the passage of disturbed solar wind, a straighter plasma tail means a steady solar wind stream, where the aberration angle between the plasma tail and the Sun–comet line is determined by the comet's velocity and ambient solar wind velocity (Swamy 2010). However, the aberration angle in the coronagraphic image is just a projection. Cheng et al. (2020) use the stereoscopic observations from STEREO to reconstruct the real position and aberration angle of the plasma tail and then infer the ambient solar wind speed. However, events with a clear plasma tail observed by two coronagraphs simultaneously are relatively rare; and selection of the projected pixels of the same target on two different coronagraphic images may be not precise enough. In this work, we develop a method using a single-view observation of the plasma tail to infer the ambient solar wind speed, which will have a wider prospect of application. In Section 2, we will describe the observations used in this work and how to reconstruct the plasma tail from the single-view coronagraphic images in three-dimensional space. In Section 3, we will analyze the results and compare

them to results from other methods. In Section 4, we will draw a brief conclusion and discuss the feasibility of our method.

2. Observations and Measurements

The instruments that provide coronagraphic observations of comets mainly include C2 and C3 on the SOHO spacecraft, and COR2 and HI1 on the two STEREO spacecraft. In this work, we investigate two cases in Cheng et al. (2020), which are the comets C/2011 W3 (Lovejoy) and C/2012 S1 (ISON). The comet C/2010 E6, which was also in Cheng et al. (2020), is not selected for the study here, because the whole comet is small and the plasma tail is short and mixed with the dust tail, which may cause notable uncertainty in determination of the direction of the plasma tail in the single-view method. Some key observational information on the two comets used in this work is listed in Table 1, including the durations of observations in the different instruments and the range of the comets' positions during each period, which are calculated from the comets' ephemeris provided by NASA's Horizons system.

The plasma tail of comet C/2011 W3 (Lovejoy) was observed by C3, COR2-B, HI1-A, and HI1-B, as indicated by red arrows in Figure 1. The duration used in this work is from 21:54UT on 2011 December 16 to 23:29UT on 2011 December 19, during which the comet was moving away from the Sun. Its plasma tail appeared in the field of view (FOV) of C3 and COR2-B at first, and then entered the FOV of HI1. The periods when the plasma tails were observed by two instruments simultaneously are the period from 21:54UT on 2011 December 16 to 06:24UT on 2011 December 17 in the FOVs of C3 and COR2-B, and the period from 12:09UT on 2011 December 17 to 23:29UT on 2011 December 19 in the FOVs of HI1-A and HI1-B. The two periods were used for the dual-view reconstruction by Cheng et al. (2020).

The plasma tail of comet C/2012 S1 (ISON) was distinct from the dust tail in the FOVs of COR2-A and COR2-B. Figure 2 show some example coronagraphic images of the comet. The durations of the plasma tail in the two COR2 FOVs are similar, being from 14:39UT to 16:54UT on 2013 November 28 in COR2-A and from 14:54UT to 17:54UT in COR2-B. The overlap was used for the dual-view reconstruction in the study of Cheng et al. (2020) too.

2.1. Autorecognition of Plasma Tails

Reconstruction of the plasma tail in three-dimensional (3D) space requires its recognition on the coronagraphic image. In general, the comet plasma tail in a steady space environment is nearly straight and narrow in a coronagraphic image. Hence, we could manually select a set of points along the tail to determine the projected tail position and direction. Considering that manual selection lacks repeatability and reliability, we develop an auto recognition method to better identify the plasma tail.

For the coronagraphic observation of the comet at a certain time, we first obtain the coordinate of the nucleus from the comet ephemeris and then project it on the coronagraphic image to locate the pixel corresponding to the nucleus (the "nucleus pixel"). We construct a straight line starting from the nucleus pixel, and sum the brightness of the pixels on the half-line, which are determined by Bresenham's line algorithm (Bresenham 1965), as shown in Figure 3. Rotating this line by fixing its start point on the nucleus pixel, we obtain the profile of the summed brightness versus the angle between the line and the Sun–comet line. With respect to

the Sun–comet line, the rotation angle of the half-line is positive on the side where the comet's dust tail is located. We fit this curve with a double Gaussian function plus a background quadratic function. The two fitted Gaussian peaks represent the central directions of the plasma tail and dust tail. Since the plasma tail is weaker than the dust tail in white-light images, the smaller peak is recognized as the result of the plasma tail, and the corresponding angle is the projected direction of the plasma tail. The 3σ uncertainty in the Gaussian fitting of the plasma tail is used to calculate the uncertainty of the inferred solar wind speed.

It should be noted that the total brightness summed along the half-line is not always from its start point on the nucleus pixel. This treatment is for the cases in which the plasma tail near the comet's nucleus is too weak and too close to the dust tail to form a double peak in the cumulative brightness curve. The double-peak feature will appear again if we sum the brightness by skipping the pixels near the comet's nucleus, as we do for the second case, the comet C/2012 S1 (ISON), in Figure 5.

2.2. Deprojection of Comet Tails

The aberration angle between the plasma tail and Sun–comet line is the key for the estimation of ambient solar wind speed. However, the aberration angle on the coronagraphic image is the projection angle that deviates from the true angle. Cheng et al. (2020) used stereoscopic observations to reconstruct the 3D direction. In this work, we obtain the 3D direction from the single-view observation based on a simple but reasonable assumption, as described below.

The plasma velocity along the tail is the vector difference of the solar wind velocity and comet's orbital velocity. Since the comet moves in an orbital plane around the Sun, its velocity is in the orbital plane. Assuming that the solar wind flows radially, i.e., the azimuthal and elevation components of the solar wind velocity are negligible, we can infer that the comet plasma tail must be in the orbital plane. This assumption is reasonable for a steady background solar wind at a distance not too close to the Sun (Weber & Davis 1967; Kasper et al. 2019). Hence, if we consider a certain point P on the plasma tail, the projection point P′ on the coronagraphic image is the intersection between the observer–P line and the plane of the sky that is perpendicular to the observer–Sun line. Conversely, if we first get the coordinate of P′ in the coronagraphic image, then we can derive the coordinate of P from the intersection between the observer–P′ line and the comet's orbital plane. Finally, we have the real 3D direction of the plasma tail as the vector from the comet's nucleus to P.

3. Analysis and Results

Once we have the position and velocity of the comet's nucleus from its ephemeris and obtain the vector of the plasma tail from the single-view coronagraphic observation, we can derive the ambient solar wind speed using the formulae of Cheng et al. (2020). We repeat the above procedure for every time stamp to obtain the variation of the ambient solar wind speed.

3.1. Comet C/2011 W3 (Lovejoy)

Figure 4 shows the estimated solar wind speed around the comet C/2011 W3 (Lovejoy) from the different coronagraphs: C3 (red solid), COR2-B (green solid), HI1-A (magenta solid), and HI1-B (cyan solid). During the period of observations, the

Table 1
Observations of the Comets C/2011 W3 (Lovejoy) and C/2012 S1 (ISON) in the FOV of Different Instruments

Comet	Observations	Start Time	End Time	Initial Position				Final Position			
				Radial Distance (R_s)	Longitude (deg)	Latitude (deg)	Angle (deg)	Radial Distance (R_s)	Longitude (deg)	Latitude (deg)	Angle (deg)
C/2011 W3 (Lovejoy)	C3	2011/12/ 16 21:54	2011/12/ 17 15:55	20.95	50.10	−23.83	42.58	31.92	45.38	−27.01	44.48
	COR2-B	2011/12/ 16 21:54	2011/12/ 17 06:24	20.96	50.10	−23.83	6.19	26.41	47.41	−25.68	6.29
	HI1-A	2011/12/ 17 00:09	2011/12/ 19 23:29	22.45	49.27	−24.41	31.74	58.11	39.90	−30.31	32.99
	HI1-B	2011/12/ 17 12:09	2011/12/ 19 23:29	29.80	46.10	−26.55	6.36	58.12	39.90	−30.31	7.19
C/2012 S1 (ISON)	COR2-A	2013/11/ 28 14:39	2013/11/ 28 16:54	5.70	96.33	−64.72	61.81	3.57	172.97	−60.25	61.58
	COR2-B	2013/11/ 28 14:54	2013/11/ 28 17:54	5.44	101.86	−65.87	13.83	2.87	−159.06	−35.72	13.92

Note. Data include the start time, end time, distance, longitude, and latitude in the HCI coordinate system, which are obtained according to the comet ephemeris. The intersection angle between the satellite–comet line and the comet's orbital plane is also listed.
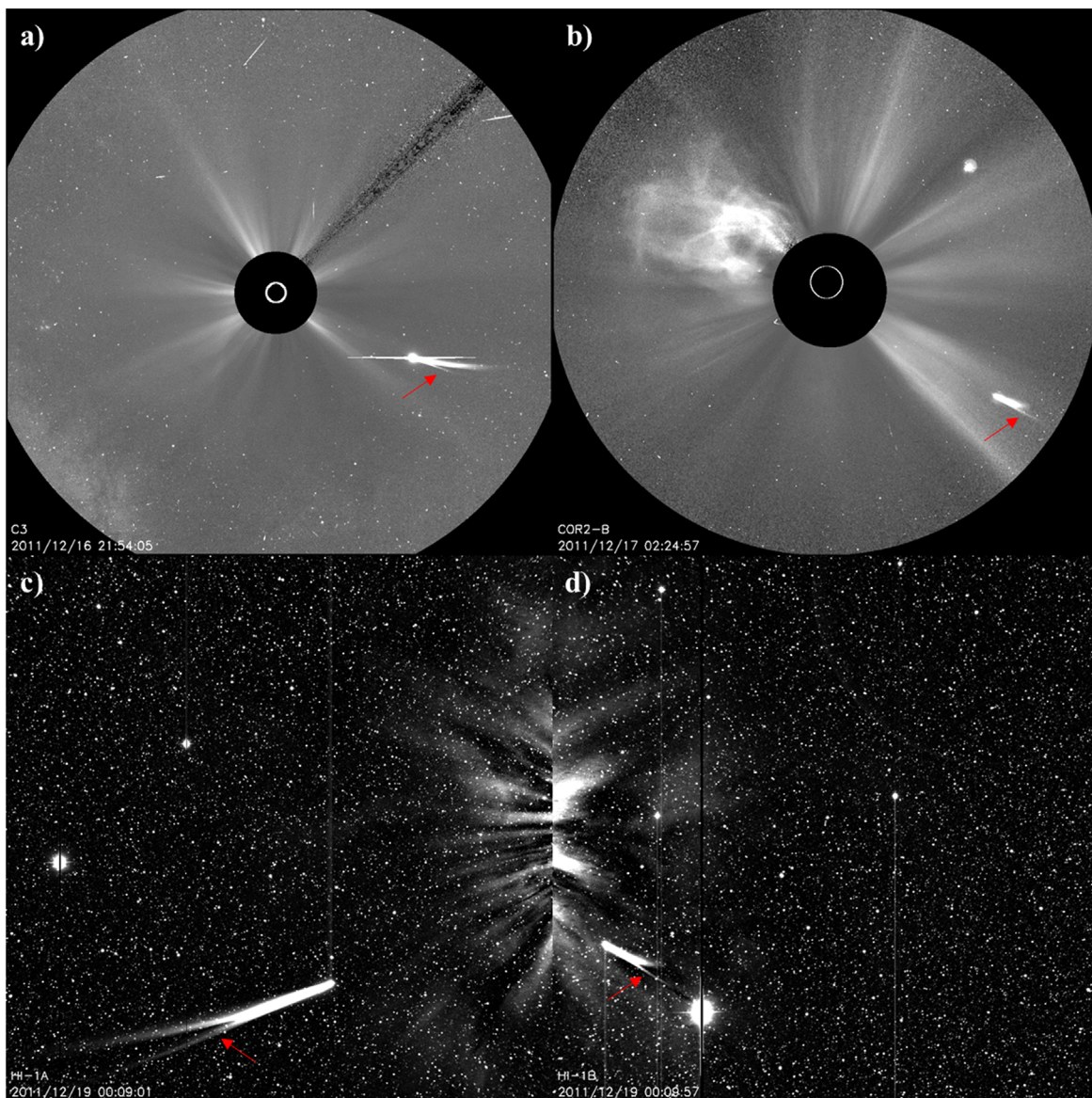
Figure 1. Comet C/2011 W3 (Lovejoy) observed by C3 (a), COR2-B (b), HI1-A (c), and HI1-B (d). The red arrows in each image point out the comet plasma tail.

comet moved away from the Sun from $\sim$20 to $\sim$60 solar radii (R_s), with the longitude ranging from $\sim$50° to $\sim$40° and the latitude ranging from about $-24°$ to $-30°$ in the heliocentric inertial (HCI) coordinates. The comet was in the low-latitude region and a quiet solar wind environment. Hence, the ambient solar wind speed is generally not high and shows no sudden change; it varies from $\sim$500 to $\sim$200 km s^{-1}.

The comet plasma tail first appeared in the FOV of C3; the comet moved from $\sim$20 to $\sim$30 R_s, where the inferred solar wind speed decreases from $\sim$500 km s^{-1} to $\sim$400 km s^{-1}. During almost the same period, the comet also appeared in the FOV of COR2-B; it moved from $\sim$20 to $\sim$26 R_s, where the inferred solar wind speed is near 300 km s^{-1}. Before the comet disappeared in the FOVs of C3 and COR2-B, it was captured by HI1-A and observed for about three days. In the FOV of HI1-A, the comet moved from $\sim$22 to $\sim$56 R_s, where the solar wind decreases from $\sim$350 to $\sim$250 km s^{-1}. During the period in the FOV of HI1-A, the comet also appeared in the FOV of HI1-B from about 12:00UT on 2011 December 17, during

which time it moved from $\sim$30 to 60 R_s and the solar wind speed varies between 200 and 300 km s^{-1}.

In the period when the comet was observed by HI1-A and HI1-B simultaneously, the solar wind speeds inferred from the two individual instruments show similar trends and are close to each other. The results from HI1-B are almost within the range of error bars of HI1-A's results. However, the results from C3 and COR2-B are inconsistent; the solar wind speed inferred from COR2-B is notably smaller than C3's result. We notice that the comet was within 30 R_s in the FOVs of C3 and COR2-B, so the assumption of radial solar wind is probably invalid. Thus, such a difference could be attributed to the presence of the non-negligible tangential component of the solar wind velocity, which will be discussed in detail in the next section.

We also plot the solar wind speeds from the dual-view method (black solid) of Cheng et al. (2020), the ENLIL model (red dotted–dashed; Odstrčil et al. 1996; Odstrcil 2003), and the heliospheric tomography with IPS data (blue dotted–dashed; Jackson et al. 1997) in Figure 4 for comparison. In general, the results from the single-view observation are consistent with
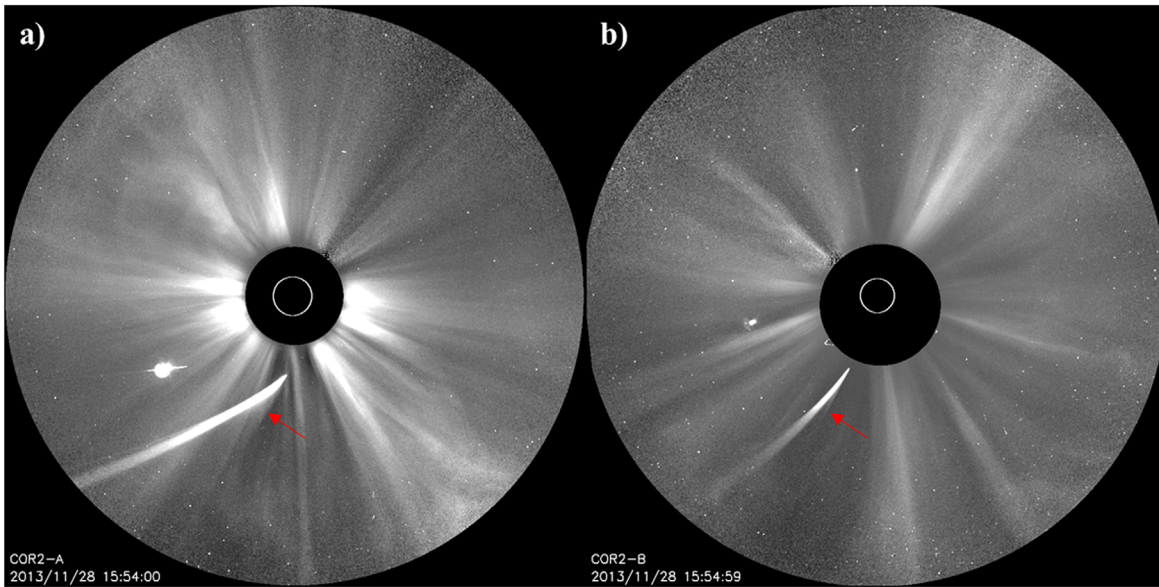
Figure 2. Comet C/2012 S1 (ISON) observed by COR2-A (a) and COR2-B (b). The red arrows in each image point out the comet plasma tail.

those from the dual-view method. Though the results from C2 and COR2-B using single-view method are different, they are comparable with the solar wind speed inferred from the dual-view method due to the large uncertainty in the latter method. When the comet was farther from the Sun and observed by HI1-A and HI1-B, the solar wind speeds inferred from the single-view method and dual-view method show similar trends. While results from the single-view and dual-view investigations show a decreasing trend, the simulations from the heliosphere model and the heliospheric tomography with IPS data give a more flattened solar wind profile, suggesting the need for an independent method based on comet plasma tails in acquiring the solar wind speed in interplanetary space.

3.2. Comet C/2012 S1 (ISON)

This comet was observed from 14:39UT to 16:54UT on 2013 November 28 by coronagraphs COR2 on the twin STEREO spacecraft. For this event, the comet plasma tail in the COR2 images is much weaker than the dust tail, which means that the profile of summed brightness does not have a clear double-peak feature. Hence, we enhance the comet tails using Sobel edge detection and accumulate the brightness along the half-line in the fan area that contains the separated tails, rather than over the whole region from the comet's nucleus to the image boundary, as shown by the green fan-shaped box in Figure 5(a). By this treatment, a double-peak feature is clearly shown in the cumulative brightness curve (Figure 5(b)). The plasma tail is located at an angle of $\sim 7°$.

Figure 6 shows the estimated ambient solar wind speed from COR2-A (red solid) and COR2-B (green solid). The periods of this comet in the FOVs of COR2-A and COR2-B are close. During this period, the comet approached the Sun from ~ 6 to ~ 3 R_s, with the longitude ranging from $\sim 100°$ to $\sim 200°$ and the latitude ranging from about $-70°$ to $-30°$. The comet was in the outer corona and moved from the high-latitude region toward the middle-latitude region, unlike the previous case, which was at latitudes less than $30°$. The estimated ambient solar wind speeds from these two coronagraphic instruments are both in the range of 100–300 km s^{-1} and decrease with

decreasing comet–Sun distance. The difference between the two profiles is small. However, they are about 150 km s^{-1} smaller than the solar wind profile from the dual-view method. Comparing to the results from corona models, e.g., the polytropic and thermodynamic models of the Magnetohydrodynamic Algorithm outside a Sphere (MAS; Linker et al. 1999), the results from the single-view method seem to be more reasonable.

4. Conclusions and Discussions

In this work, we use the direction of a comet plasma tail to infer the ambient solar wind speed near the comet. Unlike the dual-view method, we obtain the real direction of the plasma tail based on single-view observations by assuming a radial outward solar wind. In order to improve the repeatability and reliability of identifying the plasma tail, we develop an automatic recognition technique to determine the direction of the plasma tail recorded in coronagraphic images.

We apply the method to two comets observed by multiple coronagraphs. We infer the ambient solar wind speed from each single-view observation and compare it to the results from the dual-view method and some numerical models of the solar wind. The first comet, C/2011 W3 (Lovejoy), was observed by C3, COR2-B, HI1-A, and HI1-B; it was in the relatively far Sun region and close to the ecliptic plane. The ambient solar wind speeds inferred by single-view method from the images of different instruments and by dual-view method are generally consistent with each other when the comet was beyond 30 R_s. However, an inconsistency could be found between C3 and COR2-B when the comet was within 30 R_s. This is due to the presence of a notable tangential component of the solar wind velocity, breaking the assumption of a radial solar wind in our method, as shown below.

Figure 7 shows the measurements of the velocity of solar wind protons by the PSP in the ecliptic plane during its first seven encounters between 2018 August and 2021 February. From 20 to 60 R_s, the radial solar wind gradually increases from about 150 km s^{-1} to about 350 km s^{-1}, with a dynamic range of about 100 km s^{-1}. Meanwhile, the tangential velocity
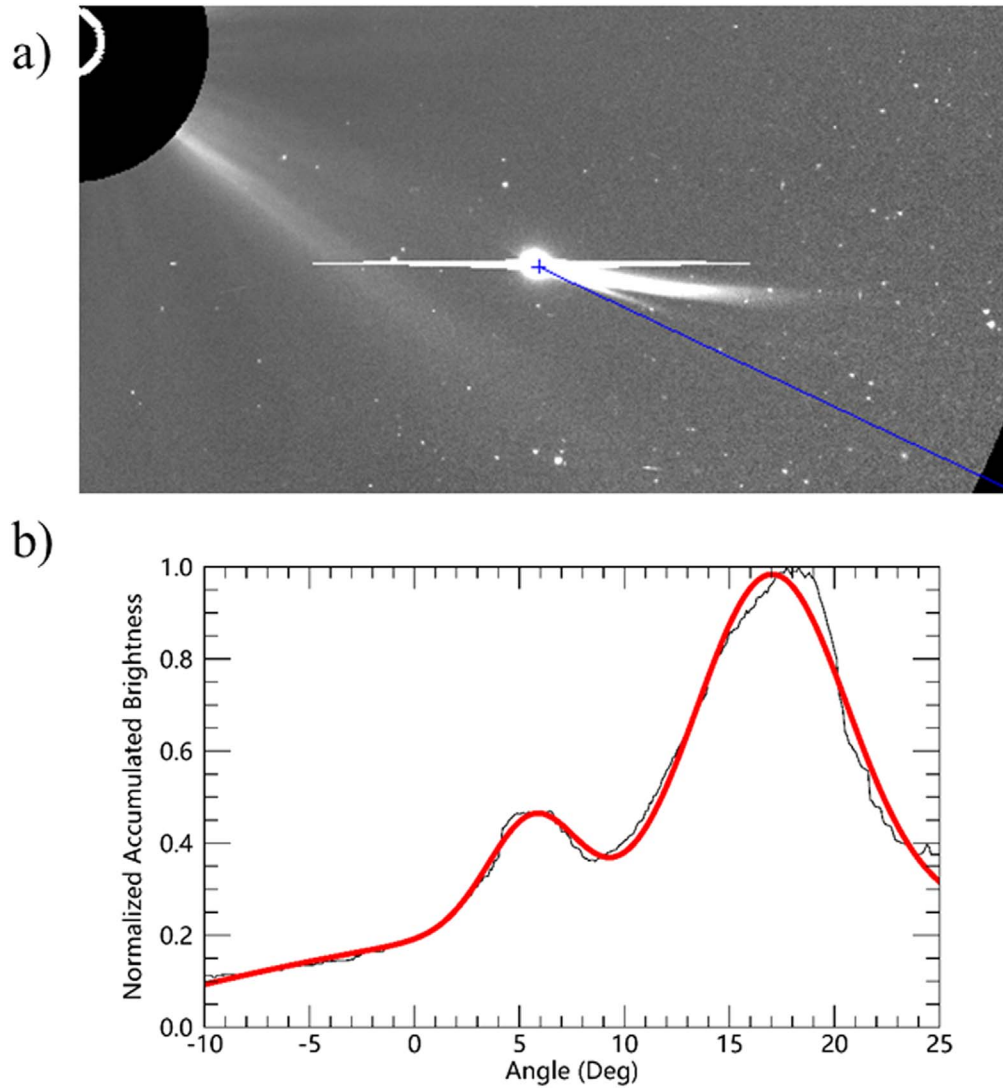
Figure 3. Illustration of the autorecognition method for the plasma tail of comet C/2011 W3 (Lovejoy). (a) The comet in the C3 image, where the blue plus symbol represents the comet's nucleus and the blue line represents the Sun–comet direction as the baseline. (b) The accumulated brightness of pixels along the line starting from the nucleus vs. the angle between the line and the baseline. The two peaks indicate the directions of the plasma tail (the lower one) and the dust tail (the higher one).

in the ecliptic plane decreases from $130 \, \mathrm{km \, s^{-1}}$ to around zero with a dynamic range of about $30 \, \mathrm{km \, s^{-1}}$, and the tangential velocity perpendicular to the ecliptic plane is negligible. The significant tangential velocity causes a notable deviation of the direction of propagation of the solar wind from the radial direction. The deviation angle could be as large as $35°$ at $20 \, R_{\mathrm{s}}$, and is larger than $10°$ up to a heliocentric distance of $35 \, R_{\mathrm{s}}$.

In order to evaluate the effect of the azimuthal angle of the solar wind velocity on the model results of the two comets' tails, we test with a nonradial propagating solar wind. For the comet C2011/W3 (Lovejoy) in the period of study, we set the radial component of the solar wind velocity to be $350 \, \mathrm{km \, s^{-1}}$ and the azimuthal angle to be θ; under this condition, we derive the real direction of the plasma tail and get its projected direction on the plane of the sky of each coronagraphic imager. Then we apply the single-view method to the plasma tail to infer the radial solar wind speed and compare it with the preset radial solar wind speed. Figure 8(a) shows the results of comparisons. It can be seen that, with increasing θ, the deviation of the solar wind speed becomes larger. For C3 and HI1-A, the deviation is relatively small, whereas for

COR2-B and HI1-B, the deviation is quite large. Especially when the θ is larger than $5°$, the projected plasma tail on the plane of the comet's orbit for COR2-B and HI1-B is on the same side as the comet's velocity, with respect to the Sun–comet line, meaning that there is no solution for the radial solar wind speed. We find that the difference in the deviations among different observers is mainly due to the intersection angle between the satellite–comet line and the plane of the comet's orbit, on which the projection effect depends. As listed in Table 1, it can be seen that the angle is only about $6°$ for COR2-B and HI1-B, whereas it is more than $30°$ for C3 and HI1-A.

The other comet, C/2012 S1 (ISON), was observed by COR2-A and COR2-B. Although it was in the near Sun region, the comet moved in the high- to mid-latitude region. Though PSP observations have shown that the azimuthal angle of the solar wind velocity is significant within $35 \, R_{\mathrm{s}}$ in the ecliptic plane, we do not yet have any knowledge about the nonradial solar wind out of the ecliptic plane. The consistency between the solar wind profiles from the two instruments implies that the assumption of radial solar wind is probably acceptable out of the ecliptic plane.
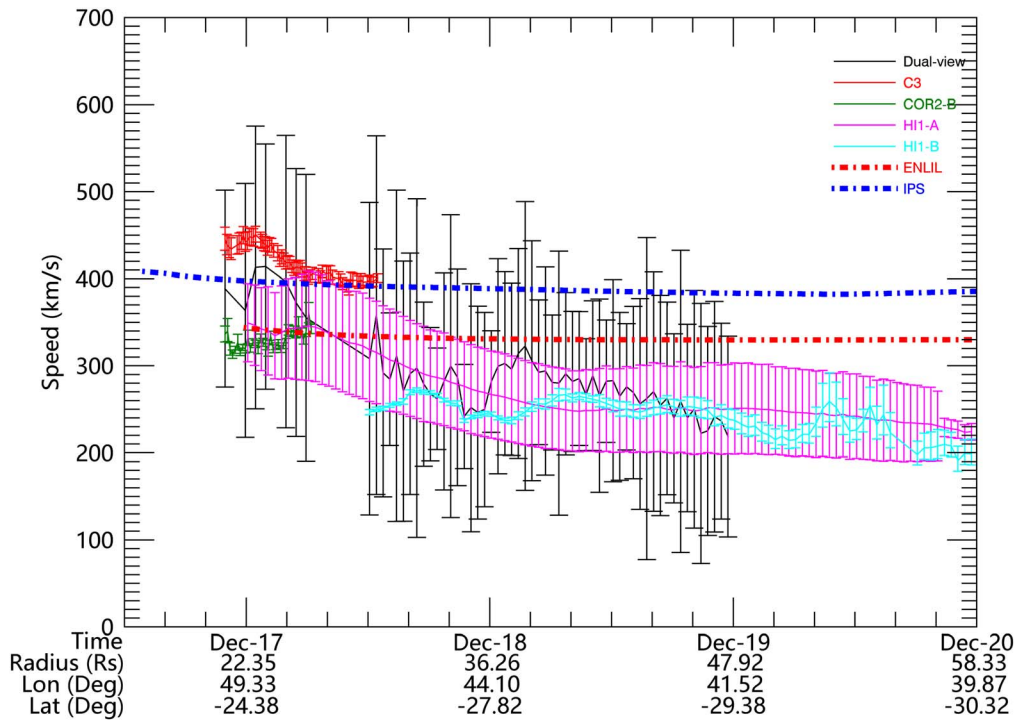
Figure 4. Ambient solar wind speeds inferred from observations of the comet C/2011 W3 (Lovejoy) in C3 (red solid), COR2-B (green solid), HI1-A (magenta solid), and HI1-B (cyan solid). Results from the dual-view method (black solid) in Cheng et al. (2020) and two solar wind models—ENLIL (red dotted–dashed) and heliospheric tomography with IPS data (blue dotted–dashed)—are also shown.
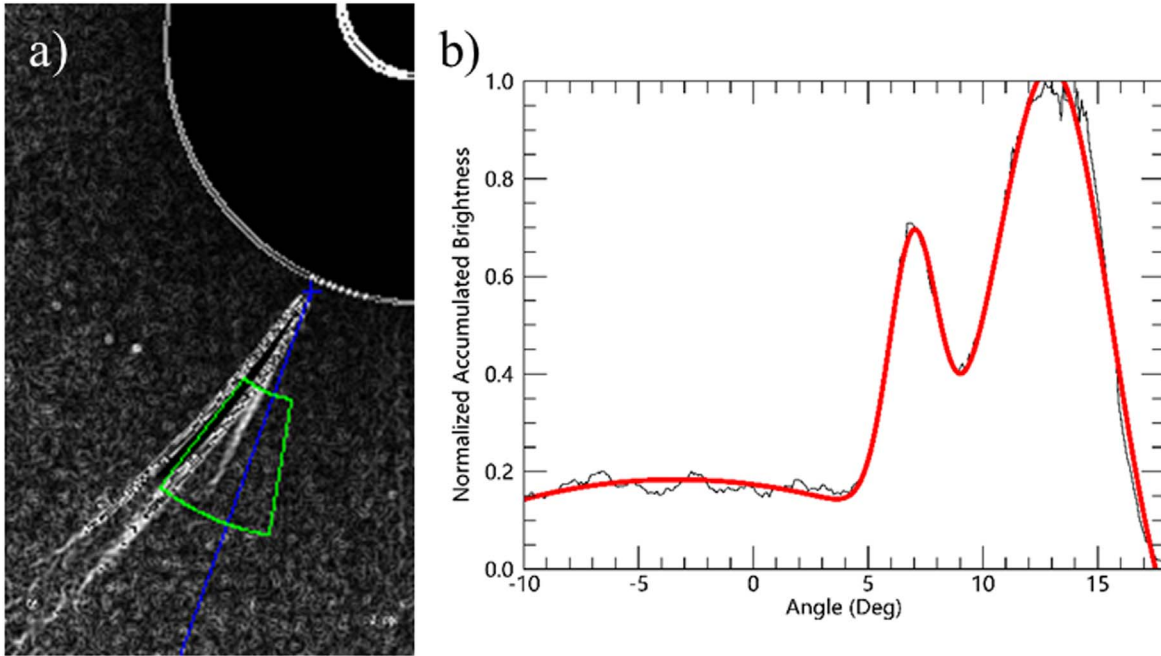

Figure 5. Similar to panels in Figure 3 but for the comet C/2012 (ISON). The comet tails are enhanced by Sobel edge detection. The green box shows the region where we accumulate the pixels' brightness along a half-line originating from the nucleus, different from that of Figure 3. The two peaks are due to the plasma tail (the lower one) and the dust tail (the higher one).

The inconsistency between the single-view and dual-view methods could be caused by various error sources. A major one is that the reconstruction of the plasma tail from dual views may be affected by the choice of corresponding pixels in the dual images, which may be not precise enough due to, for instance, (1) the synchronization in observation time and (2) the fact that the selected pixels on two images may not exactly represent the same target in 3D space.

Similarly, the test results of the azimuthal angle of solar wind velocity for this comet are shown in Figure 8(b). Here, we preset a solar wind with a radial component of $200\,\mathrm{km\,s^{-1}}$ and a varying azimuthal angle. The deviation of the inferred radial
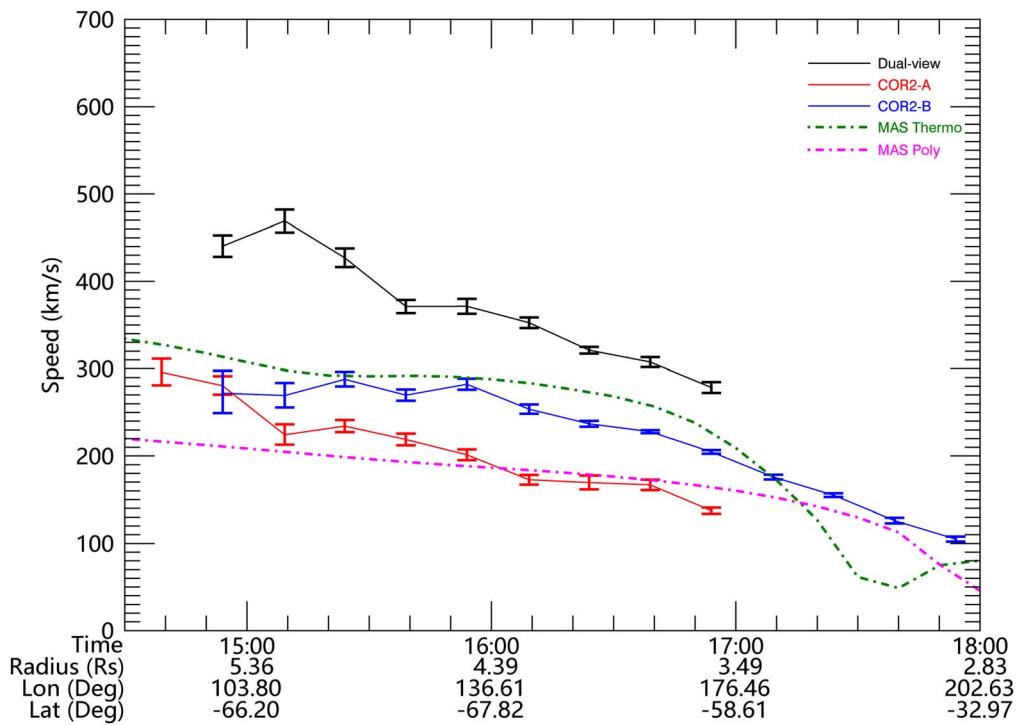
Figure 6. The ambient solar wind speeds inferred from observations of the comet C/2012 S1 (ISON) in C3 (red solid), COR2-B (green solid), HI1-A (magenta solid), and HI1-B (cyan solid). Results from the dual-view method (black solid) in Cheng et al. (2020) and two solar wind models—ENLIL (red dashed) and heliospheric tomography with IPS data (blue dashed)—are also shown.
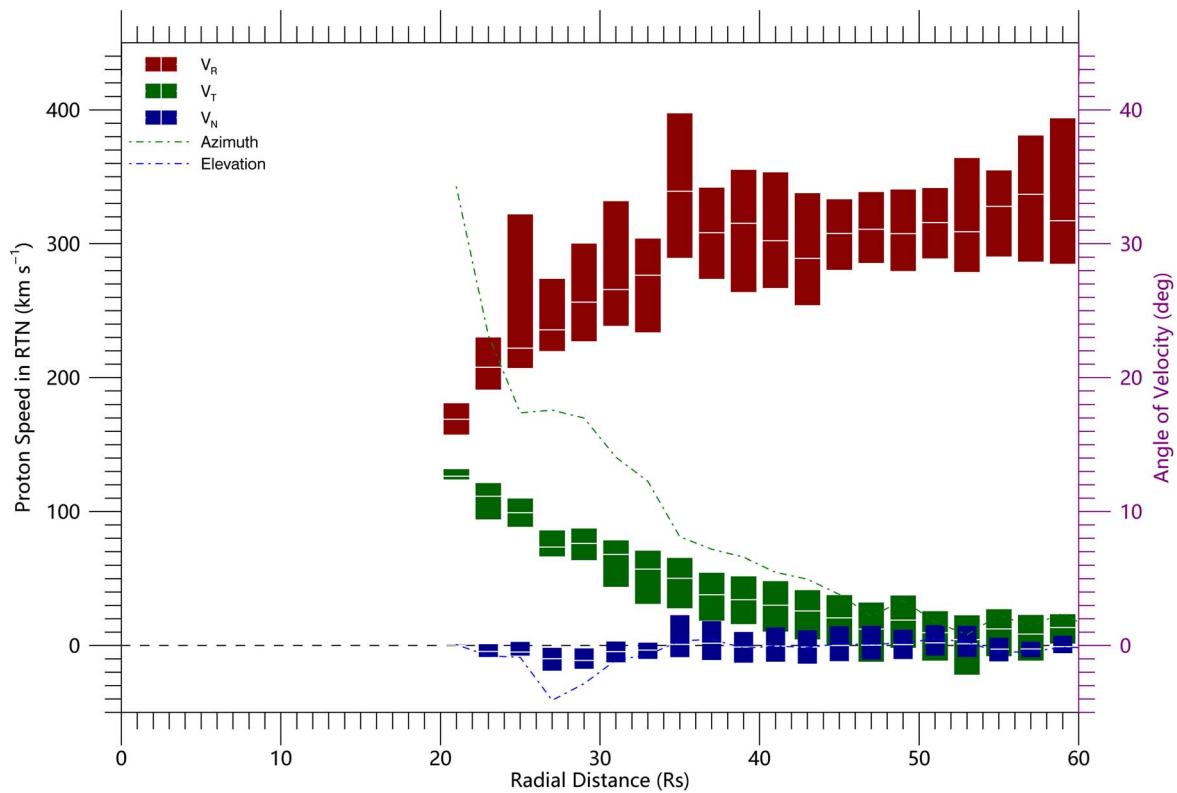

Figure 7. Measurements of the speed of solar wind protons by the Parker Solar Probe near the ecliptic plane during its first seven encounters. The data set is in the radial–tangential–normal heliospheric reference frame of the PSP. Statistics of the solar wind speed are presented as lower quartile to upper quartile bars with the median values shown by the white lines. The plot is generated based on bins of 2 R_s in the radial distance with at least 10,000 points in each bin. Dotted–dashed lines indicate the median of azimuthal (green) and elevation (blue) angles of the velocity where measurements for the three components are all made.
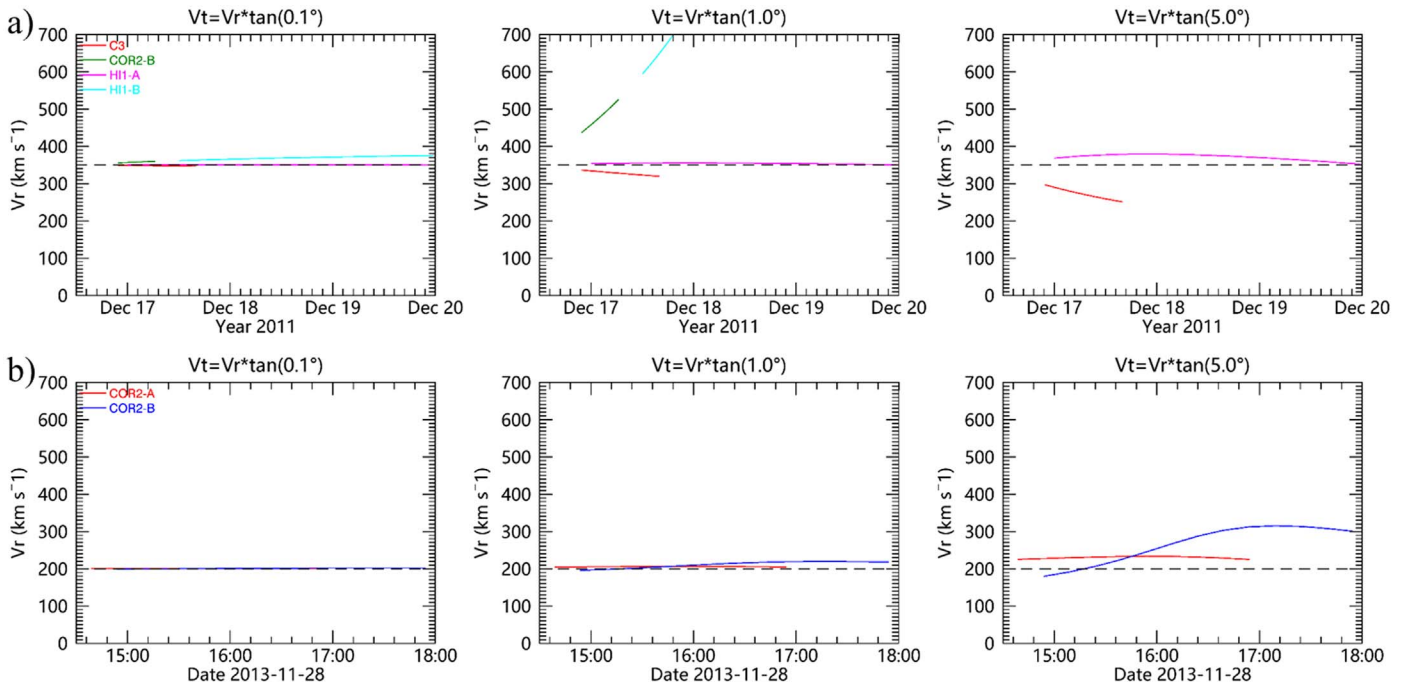
Figure 8. The radial solar wind speed inferred from single-view method based on the preset solar wind condition, with different azimuthal angles of the solar wind velocity, for (a) comet C/2011 W3 and (b) comet C/2012 S1. The dashed lines represent the preset radial solar wind speed and the colored lines indicate the referred radial solar wind speed. Columns from left to right show results for solar wind azimuthal angle of $0\overset{\circ}{.}1$, $1°$, and $5°$.

solar wind speed increases with increasing azimuthal angle. Since the intersection angle of COR2-B is about $14°$, much smaller than that of COR2-A, $62°$, the radial solar wind speed inferred from COR2-B has a larger deviation from the real one than that from the COR2-A.

Based on the above analysis, we may conclude that the single-view method is valid when (1) the observer's sight intersects the plane of the comet's orbit at a high angle and (2) the ambient solar wind velocity is near radial. In the first event, both conditions are not well satisfied for COR2-B and one of the two conditions is not well satisfied for C3 and HI1-B. Thus, the solar wind speed inferred from HI1-A should be more reliable. For the second event, COR2-A matches the first condition better than COR2-B and therefore results from COR2-A should be more reliable.

The single-view results of both comets are also compared to the model results. For comet C/2011 W3 (Lovejoy), the decreasing trend of the solar wind speed profile does not appear in the model. For comet C/2012 S1 (ISON), the single-view results are quite consistent with the model results. Models just show a kind of average solar wind speed, whereas the comet plasma tails reflect instantaneous solar wind speed. Compared to the solar wind speed measured by PSP, which shows a dynamic range of about $50–100\,\mathrm{km\,s^{-1}}$, the difference between them for this case is about $100\,\mathrm{km\,s^{-1}}$, which falls in a reasonable uncertainty range considering the dynamic range of the measured solar wind by PSP shown in Figure 7.

In summary, our single-view method is feasible for inferring the ambient solar wind speed where its tangential speed is negligible, i.e., in regions far away from the Sun or probably in regions out of the ecliptic plane, and when the observer is high above the plane of the comet's orbit. This method provides a potentially useful tool to estimate the solar wind speed around comets from only single-view imaging observations, and could be applied to observations from more solar missions, like PSP and Solar Orbiter, and ground-based telescopes. In the future, we intend to compare our method to in situ measurements when encounters between a comet and PSP or Solar Orbiter are available.

ORCID iDs

Long Cheng ⬤ https://orcid.org/0000-0003-0578-6244
Yuming Wang ⬤ https://orcid.org/0000-0002-8887-3919

References

Acuña, M. H., Ogilvie, K. W., Baker, D. N., et al. 1995, SSRv, 71, 5
Bisi, M. M., Jackson, B. V., Buffington, A., et al. 2009, SoPh, 256, 201
Bolton, S. J., Lunine, J., Stevenson, D., et al. 2017, SSRv, 213, 5
Bresenham, J. E. 1965, IBM Syst. J., 4, 25
Buffington, A., Bisi, M. M., Clover, J. M., et al. 2008, ApJ, 677, 798
Cheng, L., Zhang, Q., Wang, Y., Li, X., & Liu, R. 2020, ApJ, 897, 87
Chicarro, A., Martin, P., & Trautner, R. 2004, in ESA Special Publication 1240, Mars Express: The Scientific Payload (Noordwijk: ESA)
Cho, I.-H., Moon, Y.-J., Nakariakov, V. M., et al. 2018, PhRvL, 121, 075101
Clover, J. M., Jackson, B. V., Buffington, A., Hick, P. P., & Bisi, M. M. 2010, ApJ, 713, 394
Cranmer, S. R., Gibson, S. E., & Riley, P. 2017, SSRv, 212, 1345
DeForest, C. E., Matthaeus, W. H., Howard, T. A., & Rice, D. R. 2015, ApJ, 812, 108
Domingo, V., Fleck, B., & Poland, A. I. 1995, SoPh, 162, 1
Downs, C., Linker, J. A., Mikić, Z., et al. 2013, Sci, 340, 1196
Fox, N. J., Velli, M. C., Bale, S. D., et al. 2016, SSRv, 204, 7

Hansteen, V. H., & Leer, E. 1995, JGR, 100, 21577
Jackson, B. V., Hick, P. L., Kojima, M., & Yokobe, A. 1997, PCE, 22, 425
Jakosky, B. M., Lin, R. P., Grebowsky, J. M., et al. 2015, SSRv, 195, 3
Kaiser, M. L. 2005, AdSpR, 36, 1483
Kasper, J. C., Bale, S. D., Belcher, J. W., et al. 2019, Natur, 576, 228
Li, X., Wang, Y., Guo, J., Liu, R., & Zhuang, B. 2021, A&A, 649, A58
Linker, J. A., Mikić, Z., Biesecker, D. A., et al. 1999, JGR, 104, 9809
Matson, D. L., Spilker, L. J., & Lebreton, J. P. 2002, SSRv, 104, 1

Odstrcil, D. 2003, AdSpR, 32, 497
Odstrčil, D., Smith, Z., & Dryer, M. 1996, GeoRL, 23, 2521
Ogilvie, K. W., & Desch, M. D. 1997, AdSpR, 20, 559
Stone, E. C., Frandsen, A. M., Mewaldt, R. A., et al. 1998, SSRv, 86, 1
Swamy, K. S. K. 2010, Physics of Comets (Singapore: World Scientific)
Titov, D. V., Svedhem, H., Koschny, D., et al. 2006, P&SS, 54, 1279
Weber, E. J., & Davis, L. J. 1967, ApJ, 148, 217
Wenzel, K.-P., & Smith, E. J. 1992, GeoRL, 19, 1235